Supporting informations for "Simulation and measurement of stray fields for the manipulation of spin-qubits in one- and two-dimensional arrays"

Michele Aldeghi,[†] Rolf Allenspach,[†] Andriani Vervelaki,[‡] Daniel Jetter,[‡] Kousik Bagani,[‡] Floris Braakman,[‡] Martino Poggio,[‡,¶] and Gian Salis[*,†]

†*IBM Research-Zurich, Säumerstrasse 4, 8803 Rüschlikon, Switzerland*
‡*Department of Physics, University of Basel, 4056 Basel, Switzerland*
¶*Swiss Nanoscience Institute, University of Basel, 4056 Basel, Switzerland*

E-mail: gsa@zurich.ibm.com

Micromagnetic simulations

We compute the magnetization pattern with the micromagnetic simulation package Mu-Max3.[1] We set the initial magnetization state as a uniform, with the direction parallel to the external field. All the simulations neglect temperature induced magnetic fluctuations, due to the typical low-temperature operation of spin qubits ($< 4\mathrm{K}$) and their marginal effect on dephasing time.[2,3] The parameters used for each simulation mentioned in the main text are summarized in Table 1. The choice of parameter follows standard literature values[4] for the simulations of Fig. 1 and 4. For the simulations of the Fe-magnet measured with SSM (Fig. 3), we use a thickness of 50 nm, the shape shown in Fig. 2(c) and the parameters shown in Table 1. The saturation magnetization of $1.20\,\mathrm{MA/m}$ was measured by vibrating sample magnetometry on planar films grown in nominally identical conditions, see SI. We take into account MCA by defining randomly shaped and oriented crystallites with average dimension of $40\,\mathrm{nm}$ with cubic MCA $K_1 = 300\,\mathrm{kJ/m^3}$ (see main text). The size of the crystallites was extracted from AFM, SEM and XRD measurements (see SI). We also corrugate the surface of the magnets by a pattern with a 30 nm correlation length and a maximum height variation of 20 nm as measured by AFM (see SI). Once the simulation has reached the energy minimum, we convolve the data at a height of 70 nm above the magnet surface with a square filter with an edge size of 110 nm, to compensate for the finite size of the SQUID loop, and rescale the output of the simulation to match the aspect ratio of the cell size in the experiment (38 nm by 67 nm) by spline interpolation. The main axis of the micromagnet has an approximate tilt of 7° with respect to the y direction, which is taken into account in the simulation.

Micromagnet designs

The micromagnet design, the external field direction and the qubit array orientation define which field components of B should be used for EDSR drive or will contribute to the qubit dephasing. The geometries shown in SI Fig. 1(a) set the EDSR driving to use the slanting magnetic field coming from the magnets along the out-of-plane direction (z) and displace the electron wavefunction along the external magnetic field B_{ext} (y), which is parallel to the longest axis of the magnets and perpendicular to the qubit chain (x). The spatial arrangement of magnets, B_{ext} direction and qubit positions

Table 1: Parameters for the micromagnetic simulations

Figure	Material	Saturation magnetization (MA/m)	Exchange stiffness (pJ/m)	MCA (kJ/m^3)	Cell size (nm)
1	Co	1.44	30	none	10
2	Fe	1.20	21	300 (cubic)	10
3	Co	1.11	30	650 (uniaxial)	10
4	Fe	1.7	21	60 (cubic)	10 (micromagnet) 5 (nanomagnet)
4	Co	1.44	30	650 (uniaxial)	10 (micromagnet) 5 (nanomagnet)
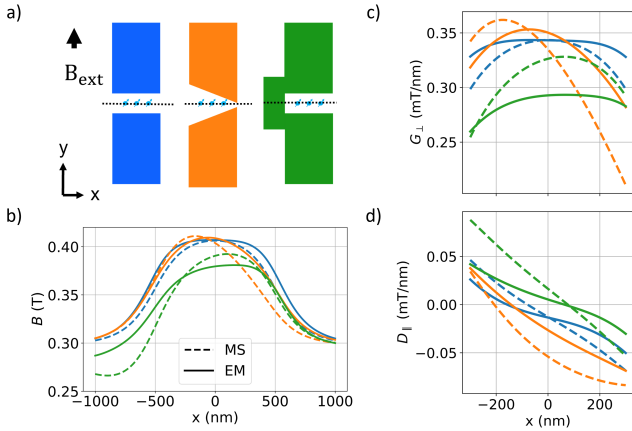
SI FIG. 1: (a) Schematic device geometry for the designs "Block" (blue), "Tapered" (orange) and "Bridge" (green) (not to scale) (b) Simulated magnetic field (B), (c) driving gradient ($G_\perp$) and dephasing gradient ($D_\parallel$) for the MS (dotted lines) and EM simulation (continuous lines) of the three designs plotted with the same color code as the sketches in (a).

sets: i) f_L should vary along the x direction, ii) the driving gradient is $G_\perp = \frac{dB_z}{dy} + \frac{dB_x}{dy}$ and iii) the dephasing gradient is $D_\parallel = \frac{dB_y}{dx} + \frac{dB_y}{dy}$. Displacement along z is neglected because we expect strongly suppressed displacements along this direction for qubits confined in semiconductor heterostructures.

The dephasing gradient is linked to the dephasing rate Γ by the charge noise induced wavefunction displacement Δ_i along the i direction, according to the equation:[5] $\Gamma = \sum_i \Gamma_i = \sum_i \pi\sqrt{2}\frac{\gamma_e}{h}\frac{dB_y}{di}\Delta i$ where γ_e is the electron gyromagnetic ratio (g-factor of 2), h Planck's constant and dB_y/di the first derivative of the stray field along the i direction. This displacement

is induced by charge noise affecting the local confinement potential.[6] Here, we assume that such displacements are identical in amplitude along the two in-plane directions x and y, but strongly suppressed along z because of the considerably stronger confinement potential along the growth direction, such that $\Gamma = \Gamma_x + \Gamma_y = \pi\sqrt{2}\frac{\gamma_e}{h}(\frac{dB_y}{dx} + \frac{dB_y}{dy})\Delta$.

We now compare three possible micromagnet designs: "Block", "Bridge"[7] and "Tapered".[8] The magnets have width $W = 1000\,$nm, length $L = 3000\,$nm, thickness $T = 200\,$nm and a variable gap G. The tapering angle is 8.5°, while the additional block for the design "Bridge" has a width $W_b = 400\,$nm and a length $L_b = 1200\,$nm. We assume the qubits to be lined up along the x direction at $y = 0$ and $z = -200\,$nm (100 nm below the edge of the magnets) and plot B along this line [SI Fig. 1(a)].

We discuss first the MS simulation and how single qubit addressability is achieved in these magnet geometries. The first design is based on two blocks with a constant gap in between [as already introduced in Fig. 1(a)], and creates a bell-shaped profile along the foreseen qubit chain position, symmetrical with respect to $x = 0\,$nm. Single qubit addressability is achieved by setting a large enough spread of the qubit frequencies with respect to the Rabi frequency ($\Delta f_L > 2 f_{Rabi}$),[7] which in this case may be achieved by placing the qubits only along $x > 0$ (< 0), such that f_L would monotonically decrease (increase) along the chain [SI Fig. 1(b)].

In the design "Tapered" the field lines are pushed outside the gap between the magnets

2

depending on the gap size, such that larger fields are found below the region where the gap is wider [SI Fig. 1(b)]. We note that this trend is the opposite from what is found at height $z = 0$.

The design "Bridge" can be decomposed into 3 magnetic dipoles, with two aligned along their longest axis and one smaller between them and displaced to the side (i.e. the additional block bridging the magnets in the "Block" geometry). The field lines connect the two opposite magnetic poles across the gap along the direction of B_{ext}, similarly to the two designs before. Likewise, also the smaller dipole on the side provides a magnetic field, but its field lines have opposite direction at the qubit location. This, combined with the stray field decay along the x direction [analogous to what was shown for the z direction in Fig. 1(d)], reduces the total field depending on the x location, creating the desired difference in f_L between the qubits [SI Fig. 1(b)]. We note that this strategy to modulate the stray field is the most successful in keeping a constant driving gradient and single qubit addressability along the x direction [SI Fig. 1(c)], in agreement with.[7]

The aforementioned considerations about single qubit addressability hold also for the EM simulation, with the important difference that the magnetization pattern relaxation lifts the symmetry of the fields assumed in the MS approximation. In the design "Block", we see that the stray field profile is flattened, due to the rotation of the magnetic field along the edge of the magnet. As forced by the vortex formation, the magnetization at $x = 0$ would point along the x direction, but the stray field minimization rotates it along the z direction [Fig. 1(b)]. The balance between these two energies changes along the edge of the magnet, such that the rotation does not happen monotonically along the xz plane facing the qubits, leading to the almost flat profile of f_L.

For the design "Tapered", the relaxed magnetization pattern results in a slightly smaller B peak that is shifted along $-x$. Also in this case the f_L difference between qubits would be smaller than expected, such that qubits placed symmetrically around the peak maxima may

have identical f_L. The same result is found in the design "Bridge", where the formation of a vortex along the surfaces in the xz planes reduces the differences in f_L between neighboring qubits. For all three designs the single qubit addressability is reduced, impacting significantly the crosstalk between them. Similarly, also the dephasing and driving gradient show significant differences between the MS and EM approach. These results highlight that the relaxation of the magnetization pattern may jeopardize the expected ESDR drive of the qubits predicted by MS simulations.

Choice of magnetic material

For a given geometry of the magnet, the magnitude of the stray field will be proportional to M_{sat}. The maximally attainable magnetic field gradient depends on the magnitude of the stray field, such that increasing M_{sat} will increase the magnetic field gradient. Since f_{Rabi} is proportional to the gradient used for the EDSR manipulation, large M_{sat} are beneficial for improving the manipulation speed.

This seemingly trivial consideration was not taken into account in the development of the first micromagnets, where Co ($M_{sat} = 1.44\,\mathrm{MA/m}$) was used.[9–11] Materials like FeCo or Fe have significantly larger M_{sat} values (1.9 MA/m and 1.7 MA/m respectively).

In the main text we have shown that MCA combined with polycrystallinity and unsaturated magnetization will lead to stray field modulations. The MCA constant of Co $K_{U,1} = 650\,\mathrm{kJ/m^3}$ is the largest among these three ferromagnetic materials, suggesting that this material will be replaced as magnetic material in future devices.

We propose Fe as replacement for Co, due to the good compromise in large M_{sat} and low $K_{C,1} = 60\,\mathrm{kJ/m^3}$. For future devices, minimization of K and maximization of M_{sat} should be aimed for, such as to improve the driving to dephasing gradient ratio. Alloying Fe with 60% Co leads to the largest M_{sat} known for a ferromagnet,[4] but its $K_{C,1} = 500\,\mathrm{kJ/m^3}$[12] also hints to large stray field modulations for polycrystalline structure. Ni and permalloy have very

low MCA energies, but their low M_{sat} will lead to small driving gradients.

Conceptually, the easiest solution to keep high M_{sat} would be to use amorphous magnets (e.g., FeCoB), such that the modulation due to MCA would be removed. This could be achieved by alloying the magnet, since E_{MCA} ($\propto K$), E_{D} ($\propto M_{\text{sat}}^2$) and E_{ex} ($\propto A_{\text{ex}}$) are all material dependent parameters. As alloying usually does not independently tune just one of these parameters there is no optimum composition of the material a priori, since the optimum qubit fidelity depends also on the combination of the charge noise experienced by the qubit and the effective displacement of its position achieved with the control gates.

Edge rounding effect
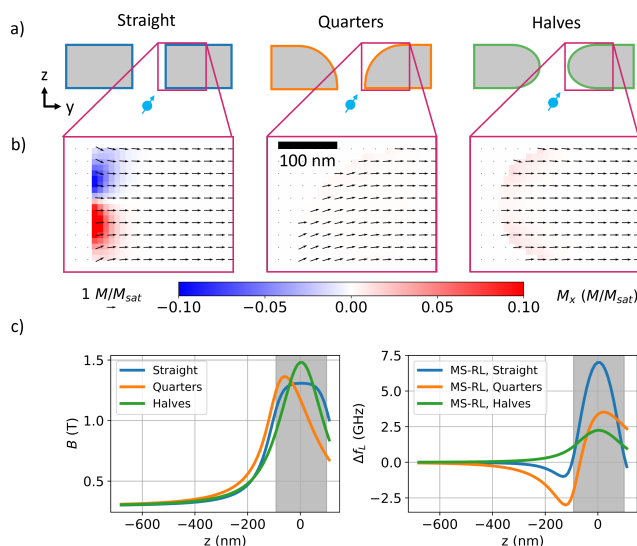
SI FIG. 2: Effect of the shape of the cross section on the stray field profile. (a) device geometry. (b) Magnetization pattern at $x{=}0$. In-plane components are shown as arrows, the out-of-plane component as color. (c) EM simulation of the magnetic field (B) (left panel) and Δf_{L} (right panel) between the MS and the EM simulations for different heights. The grey shaded areas show the position of the magnets.

Here we discuss the role of non-ideal edges of the magnetic structures, as given e.g. by lithographic processes. We use the same block geometry as in Fig. 1 with $G = 100\,\text{nm}$ and $T = 200\,\text{nm}$ (named here "Straight"), but we round the highlighted surfaces such that the $y-z$ profile is a quarter of a circle ("Quarters") or a semicircle ("Halves"). Due to the rounded shape, for both simulations higher B maxima are found with respect to the "Straight" simulation, since the magnetization pattern does almost not rotate into the x direction [SI Fig. 2(b)]. Indeed, the "Halves" shape reaches the largest stray field value in the volume between the magnets, since its magnetization pattern is almost fully aligned with the external field. For the "Quarters" shape, the induced sharp edge forces the magnetization at the surface to rotate towards the z direction, following the curvature of the rounded surface. Because of this, the stray field decreases within the gap at $z = 0$ but increases significantly for small negative z values [SI Fig. 2(c), right panel]. For the half-circle shape, the magnetization pattern keeps the inversion symmetry at $z = 0$, but due to less magnetic material at the edges the "Halves" shape provides smaller fields than the "Straight" one already at $z = -42\,\text{nm}$. Rounded edges therefore impact the magnetization pattern significantly, with differences in f_{L} of up to few GHz in comparison to straight edged magnets (e.g. the f_{L} difference between the "Straight" and "Quarters" simulation at $z = -120\,\text{nm}$ is $4.08\,\text{GHz}$).

SSM experiment

SQUID-on-lever fabrication

We fabricate a nano SQUID via Ga-FIB milling on a Nb covered AFM cantilever, as detailed in.[13] The sensor is characterized and operated at 4.2 K in a semi-voltage biased circuit, with its current response I_{SQUID} measured by a series SQUID array amplifier (Magnicon). The SQUID loop has an effective diameter of 110 nm, determined from its quantum interference pattern.

Magnetic imaging

Magnetic imaging is conducted using a custom-built scanning probe microscope under high vacuum within a ^{4}He cryostat. Since I_{SQUID}

4

modulates with the magnetic flux, this response provides a measure of the local magnetic field threading through the SQUID loop. The axis of the SQUID is tilted by 10° relative to the z direction with the tilt occurring in the x direction. This ensures that the cantilever apex (where the SQUID loop is located) can approach the sample surface without the cantilever body making contact. We scan the sample using a scanning probe controller (Specs) and piezoelectric actuators (Attocube) at a constant SQUID-sample spacing of 70 nm, measured from the magnet upper surface. The spatial resolution is given by this spacing and the effective diameter of the SQUID loop of 110 nm. During imaging, an out-of-plane magnetic field (B_z^{ext}) between 5 and 50 mT is applied to operate the SQUID near an inflection point in its interference pattern. The complete list of applied fields during the scans is shown in Table 2.

SQUID calibration

The SQUID is primarily sensitive to out-of-plane magnetic fields. However, due to the 10° tilt of the SQUID axis relative to the z-axis, a small component of the in-plane magnetic field along the y-axis can also thread through the SQUID loop. In addition, strong in-plane magnetic fields reduce the density of superconducting charge carriers in the SQUID, suppressing its current modulation. Both effects make the SQUID sensitive to in-plane fields, although the primary sensitivity to out-of-plane fields remains. To account for these effects, we measure the response of I_{SQUID} as a function of both out-of-plane applied magnetic field B_z^{ext} and in-plane applied magnetic field B_y^{ext} after each scan, over a range of ±150 mT around the applied fields used during the scans. Before each scan, the Fe nanomagnets are initialized by applying $B_y^{\text{ext}} = 800$ mT, followed by sweeping down to the field used during the scan. Since I_{SQUID} is sensitive to both in-plane and out-of-plane fields ($I_{\text{SQUID}}(B_z, B_y)$), we have to determine the stray field of the nanomagnet iteratively. Initially, we assume that in-plane field components do not affect I_{SQUID}. We hence set $B_y = 0$ at every position and solve for an ini-

tial B_z using $B_z(I_{\text{SQUID}}, B_y = 0)$ and plugging in the measured I_{SQUID}. Following $\nabla \cdot \mathbf{B} = 0$ and Maxwell's equations,[14] we use this initial $B_z(x, y)$ to solve for $B_y(x, y)$. We can then obtain a refined map of $B_z(x, y)$ by solving for $B_z(I_{\text{SQUID}}, B_y)$ at each position and plugging in the measured I_{SQUID} and the new values of B_y. We iterate in this way until the difference between successive $B_z(x, y)$ maps becomes negligible. Although an out-of-plane field is applied to operate the SQUID in the linear response region, the stray magnetic field from the nanomagnets exceeds 100 mT, pushing the calibration beyond the half-period range of the interference pattern (i.e., the region between a maximum and a minimum). Consequently, $I_{\text{SQUID}}(B_z)$ becomes multi-valued, complicating the calibration process. To address this, the multi-valued modulation curve $I_{\text{SQUID}} - B_z$ is cropped at the extrema to create out-of-plane field ranges with a monotonic response. Each pixel in the scan is assigned to a specific field region corresponding to a monotonic calibration curve $I_{\text{SQUID}} - B_z$. However, near the maxima and minima of $I_{\text{SQUID}}(B_z)$, the signal-to-noise ratio is low, resulting in noisy regions with large errors. These errors propagate to the $B_x(x, y)$ and $B_y(x, y)$ components, and the iterative calibration process cannot compensate for them. Additionally, regions with a strong B_x component also exhibit larger errors, as the calibration only considers B_z and B_y components, without accounting for the reduction in I_{SQUID} caused by strong B_x fields.

Table 2: External magnetic field applied to the micromagnet during the SSM scans.

Scan name	$B_{\text{ext}} = (B_x, B_y, B_z)$ (mT)
0.5	(500,0, -3)
0.38	(380, 0, -13)
0.1	(100, 0, -45)
0	(0, 0, -43)
-0.1	(-100, 0, -53)
-0.38	(-380, 0, 27)

Saturation magnetization measurement

We use a Lake Shore Cryotronics 7300 Series Vibrating Sample Magnetometer to determine the saturation magnetization. The sample used is a 10x10 mm^2 square and 50 nm thick blanket Fe film deposited by e-beam evaporation, under the nominally same conditions as for the growth of the micromagnet in Fig. 2. We measure an hysteresis loop by applying the external field parallel to the sample surface (i.e. within the easy plane set by shape anisotropy). We calculate the magnetization under the assumption that the whole 50 nm deposited film is magnetic, finding $M_{sat} = 1.2\,\mathrm{MA/m}$ (SI Fig. 3).
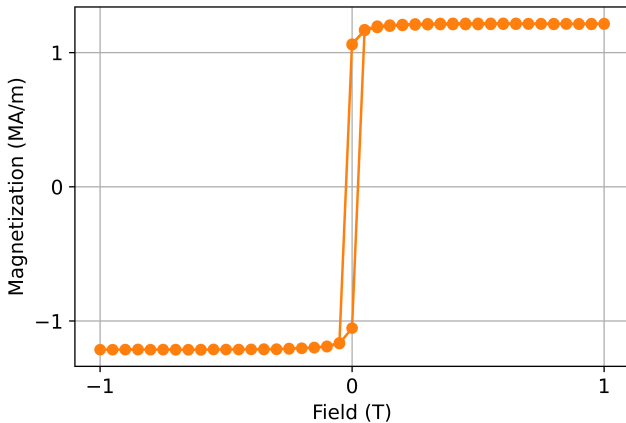
SI FIG. 3: Vibrating sample magnetometry on a blanket film of Fe. We found $M_{sat} = 1.2\,\mathrm{MA/m}$, which correspond to a 30% reduction from the literature value of $1.7\,\mathrm{MA/m}$.[4]

Crystallite size and texture determination

We investigated the crystallite size and texture of a blanket Fe film with 50 nm thickness grown in nominally identical conditions as the magnet scanned in Fig. 2, since standard XRD can be performed only on structures considerably larger than the micromagnets. We use a Panalytical X'Pert MRD tool in grazing incidence (grazing angle is 1°). The planar film is polycrystalline and shows no texture, as confirmed by the XRD scan and a rocking curve performed along the incident beam direction (SI Fig. 4). We plot the full-width at half maxima (FWHM) of the peaks angle dependence after correcting for the instrumental broadening in the Williamson-Hall plot. The scattering of the data points is considerably larger than the uncertainties due to the peak fitting, invalidating the assumptions used for extracting strain and crystallite size in the conventional Williamson-Hall analysis. Such deviations are caused by anisotropic crystallites, as visible in the SEM figure [SI Fig. 5(a)]. Under the drastic assumption of uniform strain within the film, we can still try to extract a lower boundary for the crystallite size. We roughly estimate the strain ϵ using the formula $\epsilon = (\alpha_{\mathrm{Fe}} - \alpha_{\mathrm{Si}})\Delta T$, where $\alpha_{\mathrm{Fe,Si}}$ is the coefficient of thermal expansion of Fe respectively Si and ΔT the temperature difference between measurement temperature and the deposition temperature, which we estimate to be 200 K. We calculate then a strain of 0.182%, and under this strain assumption we find that a value of approximately 11 nm for the crystallite size fits best. This crystallite size is in agreement with the smallest side of the elongated crystallites measured in the SEM images.

Surface roughness measurement

We performed AFM measurements (Park Systems, NX20) on the micromagnet scanned in Fig. 2, finding a correlation length of 32.34 nm and a RMS roughness of 1.14 nm (SI Fig. 5). Immediately afterwards and with the same AFM tip we scanned a 50 nm thick planar Fe film grown in nominally identical conditions as the micromagnet. For the planar film the correlation length is 13.76 nm and the RMS roughness is 1.28 nm. The surface pattern visible in the SEM picture is similar, but the correlation length differs. We ascribe this difference to remaining traces of resist after the development following the electron beam lithography. Based on the SEM findings, we see in both images that grains are elongated, with a short side of approximately 10 nm and a long side ranging between 30 and 50 nm. We then assume a crystallite size of 40 nm for the simulations described in the main text.
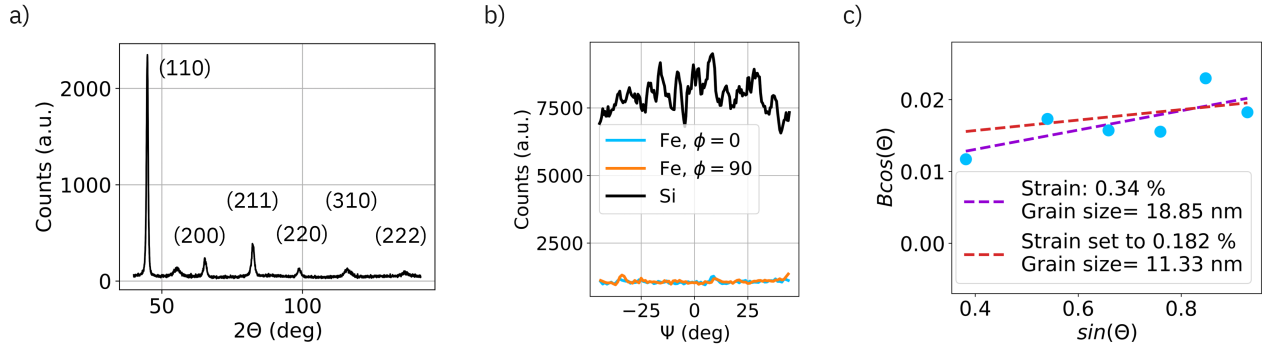
SI FIG. 4: (a) Grazing incidence XRD measurement, with the crystalline plane index reported next to the peak. (b) Rocking curve measurement along Ψ, such as to keep the grazing incidence angle scan constant. The curve labeled Si belongs to a Si polycristalline sample with known random texture. (c) Williamson-Hall plot with the peaks FWHM extracted from the measurement shown in Fig. 4(a). The dashed curve in violet is the best fit for the data points. The red dashed curve is the best fit under the assumption of a uniform strain of 0.182% throughout the film.

Gradient extraction

As explained in the main text, the micromagnets are designed to provide a large field gradient at the qubit location to perform EDSR drive. During spin qubit experiments, it is challenging to quantify the exact magnetic field gradient, since the experimentally measurable Rabi frequency (f_{Rabi}) is weighted also by the wavefunction displacement (Δ):[15] $f_{\mathrm{Rabi}} = \frac{g\mu_B G_\perp}{h} \cdot \Delta$. SSM provides a direct method to measure the driving gradient $G_\perp$. In this geometry $G_\perp = dB_z/dy$, such that the gradient can be extracted by taking the numerical derivative along the y direction of B_z. The result of this simple approach is shown in SI Fig. 6. Unfortunately, the experimental data show a high noise level in the gap region, especially at $|B_{\mathrm{ext}}| > 100\,\mathrm{mT}$ [SI Fig. 6(a)]. In the attempt to remove the experimental noise, we fit a 8th degree polynomial along the y direction to each linescan between $y = \pm1000\,\mathrm{nm}$ [one representative dataset is shown in Fig. 2(c)]. The results of the fit are shown in Fig. 2(e). SI Fig. 6(a) shows an overview of all performed scans under the conditions reported in Table 2, and Fig. 6(b) the numerical derivative of these scans.

Variable gap magnet design

We mimic the magnet design of Philips et al.[11] in our simulations by setting a width $W = 1000\,\mathrm{nm}$, length $L = 5000\,\mathrm{nm}$ and thickness $T = 200\,\mathrm{nm}$, and approximate the triangular cross-section of the magnet edges as a staircase with a height of 200 nm, a base of 100 nm and the step edge matching the cell size of 10 nm. We also take into account a 40 nm misalignment along the x direction between the two magnets. The gaps are set to 280 nm and 430 nm. We show an overlayed image of our simulation design and a SEM image of a sample made in the same fabrication run as the one used in the experiment in[11] in SI Fig. 7. From the SEM image a granular structure with features size of approximately 40 nm is visible. We thus use a crystallite size of 40 nm in the simulations described in the main text.

References

(1) Vansteenkiste, A.; Leliaert, J.; Dvornik, M.; Helsen, M.; Garcia-Sanchez, F.; Van Waeyenberge, B. The design and verification of MuMax3. *AIP Advances* **2014**, *4*, 107133.

(2) Neumann, R.; Schreiber, L. Simulation of micro-magnet stray-field dynamics for
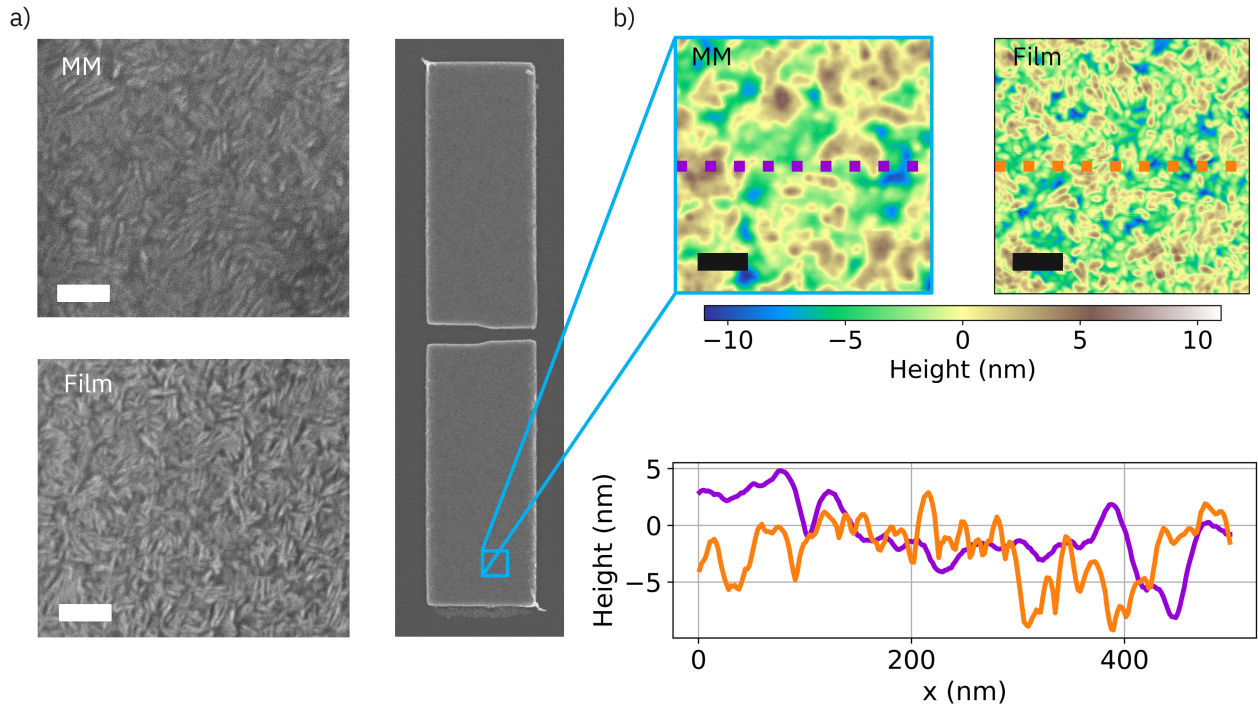
SI FIG. 5: (a) SEM images of the micromagnet scanned in Fig. 3 ("MM") and a planar Fe film grown in nominally identical conditions ("Film"). (b) AFM measurement of the same magnets, where the panel below reports the data along the cross section shown. All scale bars are 100 nm.

spin qubit manipulation. *Journal of Applied Physics* **2015**, *117*, 193903.

(3) Kha, A.; Joynt, R.; Culcer, D. Do micromagnets expose spin qubits to charge and Johnson noise? *Applied Physics Letters* **2015**, *107*, 172101.

(4) Cullity, B. D.; Graham, C. D. *Introduction to Magnetic Materials*; John Wiley & Sons, 2011.

(5) Aldeghi, M.; Allenspach, R.; Salis, G. Modular nanomagnet design for spin qubits confined in a linear chain. *Applied Physics Letters* **2023**, *122*, 134003.

(6) Connors, E. J.; Nelson, J.; Qiao, H.; Edge, L. F.; Nichol, J. M. Low-frequency charge noise in Si/SiGe quantum dots. *Physical Review B* **2019**, *100*, 165305.

(7) Yoneda, J.; Otsuka, T.; Takakura, T.; Pioro-Ladrière, M.; Brunner, R.; Lu, H.; Nakajima, T.; Obata, T.; Noiri, A.; Palmstrøm, C. J.; Gossard, A. C.; Tarucha, S. Robust micromagnet design for fast electrical manipulations of single spins in quantum dots. *Applied Physics Express* **2015**, *8*, 084401.

(8) Brunner, R.; Shin, Y.-S.; Obata, T.; Pioro-Ladrière, M.; Kubo, T.; Yoshida, K.; Taniyama, T.; Tokura, Y.; Tarucha, S. Two-Qubit Gate of Combined Single-Spin Rotation and Interdot Spin Exchange in a Double Quantum Dot. *Physical Review Letters* **2011**, *107*, 146801.

(9) Pioro-Ladrière, M.; Obata, T.; Tokura, Y.; Shin, Y. S.; Kubo, T.; Yoshida, K.; Taniyama, T.; Tarucha, S. Electrically driven single-electron spin resonance in a slanting Zeeman field. *Nature Physics* **2008**, *4*, 776–779.

(10) Watson, T. F.; Philips, S. G.; Kawakami, E.; Ward, D. R.; Scarlino, P.; Veldhorst, M.; Savage, D. E.; Lagally, M. G.; Friesen, M.; Coppersmith, S. N.; Eriksson, M. A.; Vander-

sypen, L. M. A programmable two-qubit quantum processor in silicon. *Nature* **2018**, *555*, 633–637.

(11) Philips, S. G.; Madzik, M. T.; Amitonov, S. V.; de Snoo, S. L.; Russ, M.; Kalhor, N.; Volk, C.; Lawrie, W. I.; Brousse, D.; Tryputen, L.; Wuetz, B. P.; Sammak, A.; Veldhorst, M.; Scappucci, G.; Vandersypen, L. M. Universal control of a six-qubit quantum processor in silicon. *Nature* **2022**, *4*, 919–924.

(12) Bozorth, R. M. *Ferromagnetism*; IEEE Press, 1993.

(13) Wyss, M.; Bagani, K.; Jetter, D.; Marchiori, E.; Vervelaki, A.; Gross, B.; Ridderbos, J.; Gliga, S.; Schönenberger, C.; Poggio, M. Magnetic, thermal, and topographic imaging with a nanometer-scale SQUID-on-lever scanning probe. *Physical Review Applied* **2022**, *17*, 034002.

(14) Broadway, D.; Lillie, S.; Scholten, S.; Rohner, D.; Dontschuk, N.; Maletinsky, P.; Tetienne, J.-P.; Hollenberg, L. Improved Current Density and Magnetization Reconstruction Through Vector Magnetic Field Measurements. *Physical Review Applied* **2020**, *14*, 024076.

(15) Kawakami, E.; Scarlino, P.; Ward, D. R.; Braakman, F. R.; Savage, D. E.; Lagally, M. G.; Friesen, M.; Coppersmith, S. N.; Eriksson, M. A.; Vandersypen, L. M. Electrical control of a long-lived spin qubit in a Si/SiGe quantum dot. *Nature Nanotechnology* **2014**, *9*, 666–670.
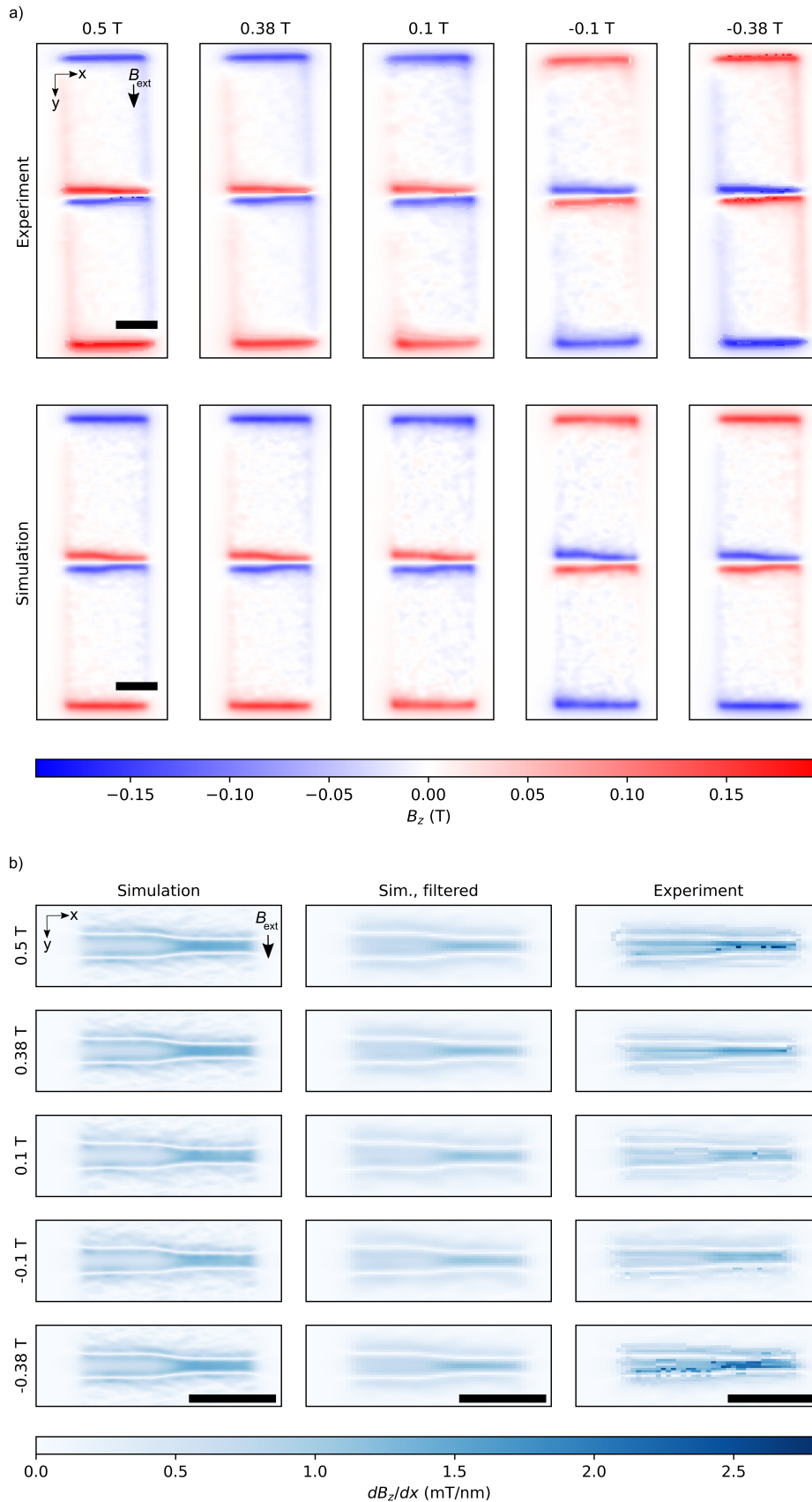
SI FIG. 6: (a) SSM scans of $B_z(x, y)$ at different external magnetic fields (upper panel) and corresponding micromagnetic simulations (lower panel). (b) Numerical derivative dB_z/dx in the region of the gap in (a); the first column shows the unprocessed simulation, the second column depicts the data of the first column smoothed with a uniform filter with 110 nm in size as to mimic the averaging performed by the SQUID loop, and the last column shows the processed SSM measurements at different B_{ext}. The scale bars are 1000 nm.
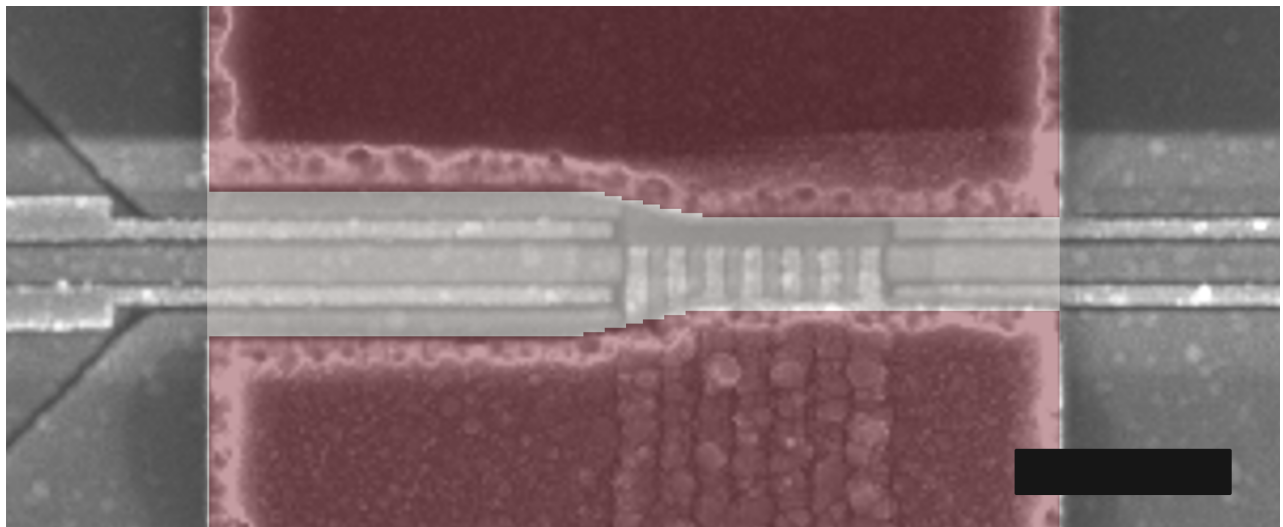
SI FIG. 7: Overlay of our simulated magnet design (red) with an SEM image of a sample made in the same fabrication run as the one described in[11] (greyscale). The scale bar is 500 nm. SEM image courtesy of Lieven Vandersypen (TU Delft) and TNO.